Evaluating the Effect of Post-Processing Steps When Analyzing Cardiac Diffusion Tensor Data

Tyler E. Cork[1,2,3,4](✉), Ariel J. Hannum[1,2,3,4], Michael Loecher[1,2], Luigi E. Perotti[5], and Daniel B. Ennis[1,2,3,4]

[1] Department of Radiology, Stanford University, Stanford CA, 94305, USA
tyler.e.cork@gmail.com
[2] Division of Radiology, Veterans Administration Health Care System, Palo Alto, CA, 94305
[3] Cardiovascular Institute, Stanford University, Stanford CA, 94305, USA
[4] Department of Bioengineering, Stanford University, Stanford CA, 94305, USA
[5] Department of Mechanical and Aerospace Engineering, University of Central Florida, Orlando FL, 32816, USA

Abstract. Cardiac diffusion tensor imaging (cDTI) is an emerging method capable of characterizing the microstructural organization of both healthy and diseased myocardium. One of the challenging aspects of a cDTI study is the associated data processing due to various acquisition imperfections that can corrupt the acquired data. We sought to investigate the role of various data processing steps by evaluating an open-source cDTI data processing software, Cardiac Diffusion in Python (CarDpy). In order to achieve this goal, healthy volunteers (N=40) were imaged. Imaging data was evaluated at six incremental post-processing steps (POSTs) using the CarDpy pipeline. cDTI metrics such as mean diffusivity (MD), fractional anisotropy (FA), and helix angle range (HAR) were evaluated after each POST. Additionally, the uncertainties of MD (dMD), FA (dFA), and the primary eigenvector ($d\boldsymbol{e}_1$) were evaluated to quantify the data precision. Statistical testing was performed after each POST in a comparison with the final POST. Empirical measurements of MD displayed stable trends across all POSTs, while a decrease in FA was observed with each incremental step. HAR remained stable after the integration of the POST that incorporated image registration into the data processing pipeline. Uncertainties decreased for all metrics as each incremental POST was added. dMD, dFA, and the $d\boldsymbol{e}_1$ had minimal improvements after the POST that incorporated shot-rejection into the data processing pipeline. Overall, this study provides an in-depth analysis pertaining to the impact of image processing on cDTI metrics and their corresponding uncertainties.

Keywords: Cardiac Diffusion Tensor Imaging · Cardiac Microstructure · MRI Processing · Myocardium Characterization.

1 Introduction

The microstructure of the heart is a highly complex system that has been studied extensively in *ex vivo* research using microscopy [29,30] and diffusion tensor

imaging (DTI) [25,17,4,18,19]. The high spatial resolution of these experiments provided a great foundation for the basic understanding of the organization of the "myofibers" in the heart [31] and has allowed for physiologic quantification of myocardial diffusion properties such as mean diffusivity (MD), fractional anisotropy (FA), and the transmural orientation of the aggregate cardiomyocyte orientation known as the helix angle (HA). More recently, *in vivo* methods for obtaining DTI data have emerged and cardiac DTI (cDTI) is now a feasible approach to estimate the microstructure of the heart *in vivo*. One of the largest contributors to this advancement was the design of motion-compensated diffusion encoding gradient waveforms for spin-echo DTI sequences [10,27,2]. The ability to compensate for position, velocity, and acceleration has allowed for reasonable quantification of diffusion properties in the heart [28,22]. Without motion-compensated gradients, spin-echo cDTI overestimates the diffusion of water within myocardial tissue and exceeds the upper limit of free water diffusion, which is 2.9 $\mu m^2/ms$ at body temperature[22].

Although *in vivo* cDTI methods now exist, it remains an extremely challenging imaging technique due to its inherently low signal-to-noise ratio (SNR), tissue motion, and extended scan duration[24].Given these *in vivo* cDTI challenges, there is a need to carefully evaluate the post-processing steps that transform imaging data into local tensor-valued data in order to mitigate the effect of corrupted images or voxels, which could result in inaccurate cDTI metrics. The importance of post-processing steps has been echoed in the recent consensus statement from the Society of Cardiovascular Magnetic Resonance (SCMR) Cardiac Diffusion Special Interest Group [5].

Recently, an open-source software package for cDTI data processing, Cardiac Diffusion in Python (CarDpy) has served as a possible solution to address these imperfections. CarDpy builds off the modular framework of Diffusion in Python (DIPY) [11] and has been adapted to suit the specific needs of cDTI data with additional modules and tools. One of these tools is a built-in graphical user interface (GUI) for segmenting the left ventricle (LV). CarDpy is built with a modular design, allowing users to easily incorporate different modules based on data and user requirements. The currently available CarDpy modules include: Gibbs Unringing, Shot-Rejection, Registration, Diffusivity Filtering, Averaging, Denoising, Interpolation, and Diffusion Tensor Reconstruction. All modules allow the option of operating on magnitude cDTI data, while most of the modules also offer the option of working with complex cDTI data. These modules offer users the ability to filter out image imperfections and generate improved quantitative cDTI metrics. However, cDTI data processing is time-consuming and a thorough investigation of the impact of data processing steps has not been evaluated.

Herein, the purpose of this work was to assess the impact of cDTI data processing steps within the CarDpy software for cDTI data obtained in healthy volunteers. We evaluated the impact on quantitative cDTI metrics after six incremental post-processing steps (POSTs) to identify the direct impact of data processing on the data. Additionally, the uncertainty of each quantitative cDTI

metric was measured to identify trends in the median uncertainty values of the estimates.

2 Methods

2.1 Study Design

Forty (N=40, 39.3 ± 13.6 years old, 23 female) healthy volunteers were consented under an IRB-approved study (Stanford Administrative Panel on Human Subjects in Medical Research, Reference #FWA00000929 & #FWA00000934) and scanned using a 3T MRI (Vida Fit, Siemens) with an 18-channel body coil and a 32-channel spine coil. Volunteers were imaged at three slice positions (basal, mid-ventricular, and apical) using a free-breathing, motion-compensated ($M_0 + M_1 + M_2$), spin-echo cDTI sequence with slice following [21]. The sequence was ECG gated to acquire images in a mid-systolic cardiac frame and a single-shot, echo planar imaging (EPI) readout was used for image acquisition. The cDTI sequence used the following parameters: echo time (TE)/repetition time (TR) = 91 ms/3 × R-R interval, receiver bandwidth = 1776 Hz/pixel, echo spacing = 0.65 ms, number of signal averages (N_{avg}) = 5, field-of-view = 256 mm × 256 mm, matrix = 128 × 128, spatial resolution = 2.0 × 2.0 × 8.0 mm^3, partial Fourier factor = 6/8, parallel imaging = 2× GRAPPA [12], phase encode polarity = blip-up, diffusion b-values = 0 and 350 s/mm^2, and fifteen (15) diffusion directions resulting in a scan time of ≈80 s/slice.

2.2 Data Processing

Images for each volunteer were processed using six incremental POSTs in the CarDpy open-source software. A graphical representation of the contents and order of each POST can be seen in Fig. 1. The POSTs include:

- $POST_1$: Averaging (magnitude) to improve SNR.
- $POST_2$: Registration (affine transformation) to improve shot-to-shot correspondence.
- $POST_3$: Unringing to reduce Gibbs ringing artifacts [14,23].
- $POST_4$: Shot-Rejection to eliminate images with motion artifacts.
- $POST_5$: Diffusivity Filtering to cut-off high diffusivity values ($\geq 3\ \mu m^2/ms$) and remove corrupted pixels.
- $POST_6$: Denoising using a local principle component analysis (PCA) [20].

After each POST the data were sequentially run through the interpolation module and the diffusion tensor reconstruction module. The interpolation module used a k-space zero-filling approach [3] for interpolation (2.0 × 2.0 × 8.0 mm^3 → 1.0 × 1.0 × 8.0 mm^3) and the diffusion tensor module used a non-linear least squares diffusion tensor reconstruction [16]. MD, FA, and the primary eigenvector ($\boldsymbol{e}_1$) were extracted from the diffusion tensor reconstruction. Images were then segmented using the CarDpy segmentation GUI. Epicardium (epi) and endocardium (endo) contours of the LV were selected by utilizing multiple cDTI

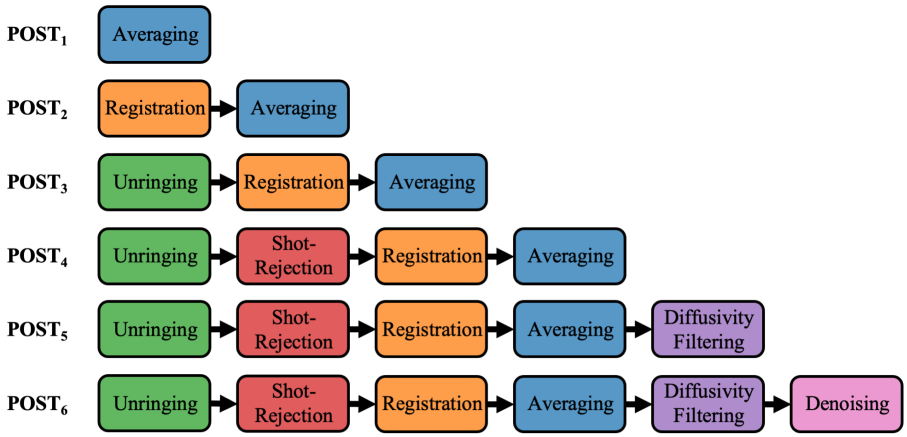

Fig. 1. An overview of each cardiac diffusion tensor imaging post-processing step (POST) from POST_1 to POST_6 (rows). For each POST, the sequential workflow of Cardiac Diffusion in Python (CarDpy) modules is displayed.

contrasts including the average diffusion-weighted images, MD maps, and the $\boldsymbol{e}_1$ RGB maps. After the segmentation was completed, the $\boldsymbol{e}_1$ was projected onto the circumferential-longitudinal plane to compute the HA. Qualitative MD, FA, and HA maps for each POST can be viewed for a volunteer at a mid-ventricular slice in Fig. 2. Additionally, incremental difference maps between sequential POSTs for all cDTI metrics are displayed in Fig. 2.

HA maps were then used to calculate each image's HA range (HAR). HAR was estimated by calculating a linear regression of all HA points within the LV for each slice, based on the normalized transmural wall thickness from epi to endo. The point at the most epicardial end of the linear regression was subtracted from the point at the most endocardial end of the linear regression, thus resulting in the HAR.

2.3 Uncertainty Measurements

Uncertainty measurements were made by generating 400 bootstraps [6] for each POST right before the averaging module; for POST_1 this means the bootstrapping was applied on the original images. Subsequently, each POST was processed through the remainder of its respective pipeline, generating 400 unique diffusion tensors. These bootstrapped tensors were then used to measure the uncertainty of MD, FA, and the $\boldsymbol{e}_1$ [13,1]. The uncertainties of MD (dMD) and FA (dFA) were measured by calculating the width of a two-sided 95% confidence interval (CI) for each voxel in the bootstrapped results. Uncertainty of the $\boldsymbol{e}_1$ ($d\boldsymbol{e}_1$) was measured by calculating the width of a one-sided 95% CI (starting from 0°) for each voxel in the bootstrapped results. Qualitative dMD, dFA, and $d\boldsymbol{e}_1$ maps

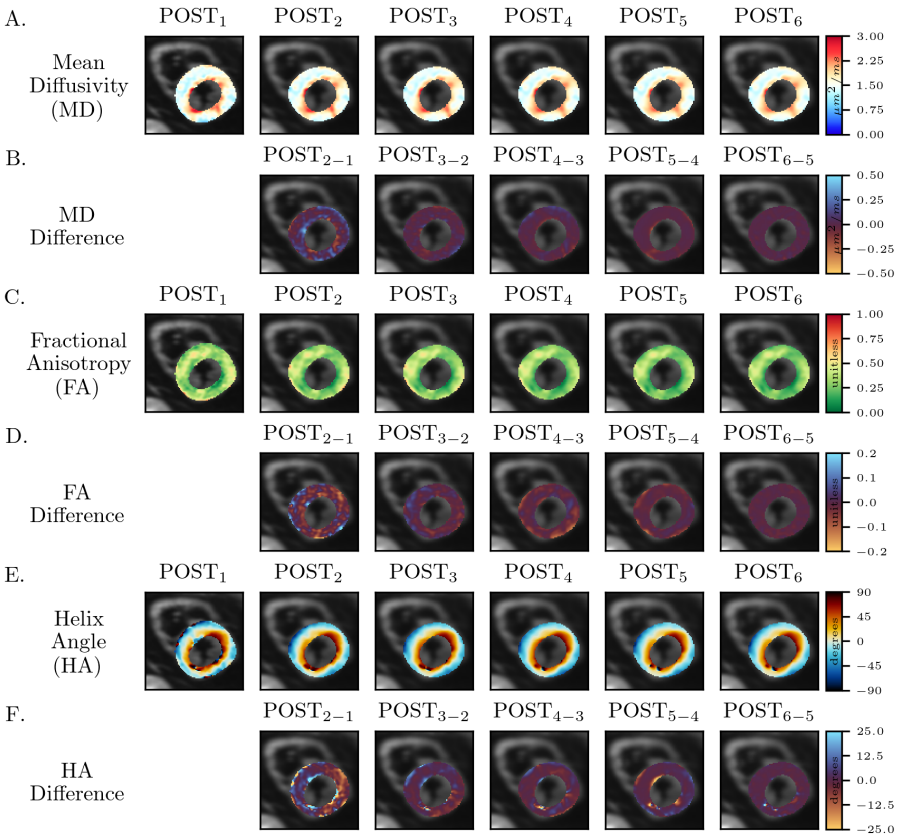

Fig. 2. Cardiac diffusion tensor imaging (cDTI) metrics are shown for a single volunteer in a mid-ventricular slice. Mean diffusivity (A), fractional anisotropy (C), and helix angle (E) maps are shown for each post-processing step (POST). The POSTs display improvements in mean diffusivity and fractional anisotropy homogeneity and helix angle coherence and smoothness from POST_1 (left column) through POST_6 (right column). Differences between consecutive POSTs for mean diffusivity (B), fractional anisotropy (D), and helix angle (F) are also displayed.

for each POST can be viewed for a volunteer at an apical slice in Fig. 3. Additionally, incremental difference maps between sequential POSTs for all cDTI uncertainties are displayed in Fig. 3.

2.4 Statistical Analysis

For each slice, the HAR and the median LV values for MD, dMD, FA, dFA, and the $d\boldsymbol{e}_1$ were reported across each POST. In Fig. 4, empirical (blue) and uncertainty (orange) measurements of cDTI metrics for all slices across all volunteers were visualized as a split violin plot for each POST. The split violin plots

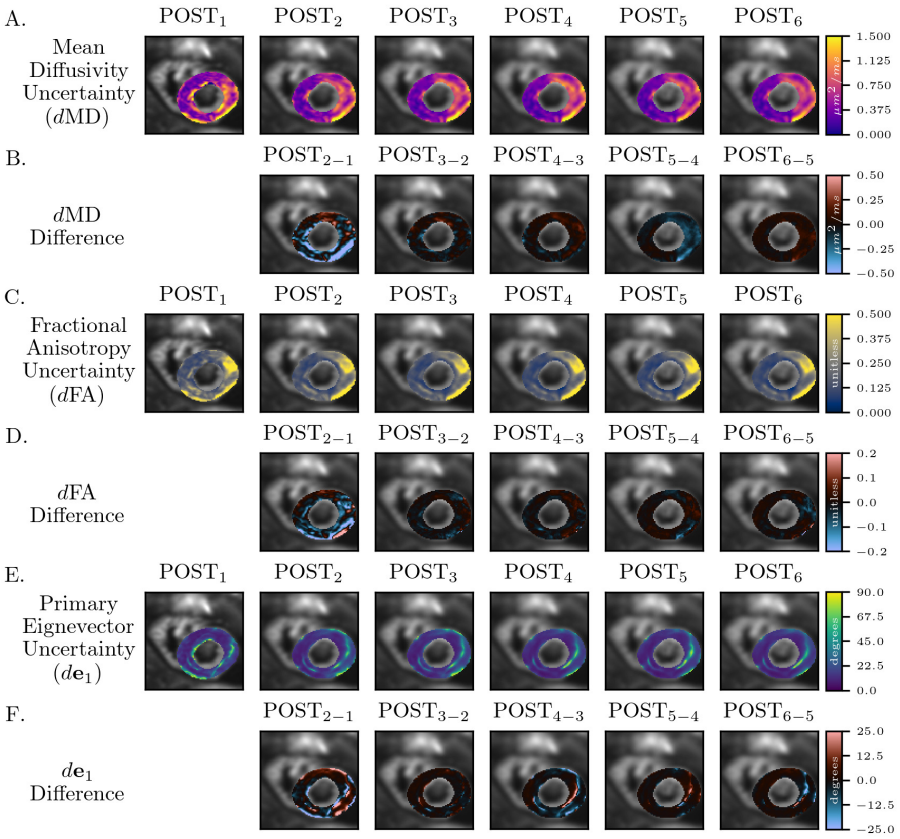

Fig. 3. Uncertainty of cardiac diffusion tensor imaging (cDTI) metrics are shown for a single volunteer in an apical slice. The uncertainty of mean diffusivity (A), fractional anisotropy (C), and the primary eigenvector (E) maps are shown for each post-processing step (POST). The POSTs display improvements in uncertainty for mean diffusivity, fractional anisotropy, and the primary eigenvector from POST_1 (left column) through POST_6 (right column). Differences between consecutive POSTs for the uncertainties of mean diffusivity (B), fractional anisotropy (D), and the primary eigenvector (F) are also displayed.

displayed the median and interquartile range (25% to 75%) for each POST. All violin plots were truncated at the limits of the data. Median values for all cDTI metics and their corresponding uncertainties can be seen in Table 1. POST_1 through POST_5 were compared to POST_6 using a paired t-tests to assess statistical significance for both cDTI metrics and the respective uncertainty in each metric. All reported p-values were evaluated after undergoing *post hoc* Holm-Šidák corrections. A p-value < 0.05 was considered significant. Statistical

signifigance results for all cDTI metics and their corresponding uncertainties can be seen in Table 2.

3 Results

Mean Diffusivity – Median MD ($\mu m^2/ms$) results remained stable across all POSTs (Table 1). When comparing MD after all other POSTs to $POST_6$, there were no significantly different findings (Table 2). Median dMD ($\mu m^2/ms$) results displayed a decreasing trend from $POST_1$ to $POST_6$ (Table 1). When comparing dMD from other POSTs to $POST_6$, we found that $POST_1$ through $POST_3$ were significantly different from $POST_6$ (Table 2).

Fractional Anisotropy – Median FA (*unitless*) results displayed a decreasing trend from $POST_1$ to $POST_6$ (Table 1). Comparisons of FA for $POST_1$ through $POST_5$ to $POST_6$ were each significantly different (Table 2). Median dFA (*unitless*) results displayed a decreasing trend from $POST_1$ to $POST_6$ (Table 1). When comparing dFA for each POST to $POST_6$, $POST_1$ through $POST_3$ were significantly different (Table 2).

Helix Angle – Median HAR (°) results increased after $POST_1$, but remained stable across all remaining POSTs (Table 1). When comparing HAR for each POST to $POST_6$, only $POST_1$ was significantly different from $POST_6$ (Table 2). Median $d\boldsymbol{e}_1$ (°) results displayed a decreasing trend from $POST_1$ to $POST_6$ (Table 1). When comparing $d\boldsymbol{e}_1$ for each POST to $POST_6$, $POST_1$ through $POST_3$ were significantly different (Table 2).

Table 1. Medians for cDTI Metrics and Uncertainties

Incremental POSTs	MD $[\mu m^2/ms]$	dMD $[\mu m^2/ms]$	FA $[unitless]$	dFA $[unitless]$	HAR [°]	$d\boldsymbol{e}_1$ [°]
$POST_1$	1.56	0.59	0.34	0.23	55.9	21.6
$POST_2$	1.59	0.56	0.32	0.20	64.7	20.4
$POST_3$	1.58	0.53	0.32	0.19	61.8	19.8
$POST_4$	1.58	0.46	0.31	0.17	63.8	16.9
$POST_5$	1.56	0.44	0.30	0.17	62.6	17.0
$POST_5$	1.56	0.46	0.29	0.16	62.0	16.6

Post-Processing Steps (POSTs)
Mean Diffusivity (MD); MD Uncertainty (dMD)
Fractional Anisotropy (FA); FA Uncertainty (dFA)
Helix Angle Range (HAR); Primary Eigenvector Uncertainty ($d\boldsymbol{e}_1$)

4 Discussion

In this study, we investigated how cDTI metrics and their respective uncertainties were affected by incremental changes in the data processing pipeline. Each

Table 2. Statistical Significance Testing for cDTI Metrics and Uncertainties

Comparisons	MD	dMD	FA	dFA	HAR	$d\boldsymbol{e}_1$
$POST_1$ vs. $POST_6$	N.S.	< 0.0001	< 0.0001	< 0.0001	< 0.05	< 0.0001
$POST_2$ vs. $POST_6$	N.S.	< 0.0001	< 0.0001	< 0.0001	N.S.	< 0.001
$POST_3$ vs. $POST_6$	N.S.	< 0.001	< 0.0001	< 0.0001	N.S.	< 0.01
$POST_4$ vs. $POST_6$	N.S.	N.S.	< 0.0001	N.S.	N.S.	N.S.
$POST_5$ vs. $POST_6$	N.S.	N.S.	< 0.05	N.S.	N.S.	N.S.

Mean Diffusivity (MD); MD Uncertainty (dMD)
Fractional Anisotropy (FA); FA Uncertainty (dFA)
Helix Angle Range (HAR); Primary Eigenvector Uncertainty ($d\boldsymbol{e}_1$)

incremental module used in this work was focused on making improvements to address artifacts in the image (Gibbs ringing, motion corrupted shots, and super-physiologic diffusivity), address shot-to-shot motion (registration), and/or improve the signal-to-noise ratio (averaging and denoising). As results from each incremental POST were computed, the uncertainty of all cDTI metrics (dMD, dFA, and the $d\boldsymbol{e}_1$) decreased, thus suggesting increased robustness in cDTI metrics estimation. In terms of uncertainty, there were significant differences from $POST_1$ through $POST_3$ when compared to $POST_6$ for dMD, dFA, and the $d\boldsymbol{e}_1$.

In summary, the median MD remained stable across all POSTs with no significant differences for all POSTs compared to $POST_6$. A decreasing trend of median FA values from $POST_1$ through $POST_6$ was observed with significant differences for all POSTs compared to $POST_6$. For median HAR, there was an 8.7° increase when comparing $POST_2$ to $POST_1$ (indicating a high impact POST) and the trend was stable thereafter. This was confirmed when analyzing the HAR for $POST_1$ vs. $POST_6$, which was significantly different, but was no longer significantly different from $POST_2$ through $POST_5$ when compared to $POST_6$. Lastly, the qualitative cDTI metric maps from $POST_1$ through $POST_6$ showed increased homogeneity for MD and FA maps, while also displaying smoother HA maps with fewer areas of discontinuity.

The median MD values reported in our study are on the higher side (1.22 - 1.68 $\mu m^2/ms$) when comparing to values typically reported in the literature for spin-echo cDTI [5]. This elevated source of MD may be partially due to the endocardial segmentation of the myocardium. In our segmentation, endocardial pixels are subject to partial voluming between the LV blood pool and myocardial tissue. The partial volumed signal appears to capture the diffusivity properties of the blood while also retaining the orientation of the myocardial tissue. Given that there is still a quantifiable orientation of the myocardium in this region, we have accepted the trade-off of elevated MD for improved HA maps. An additional possible source of these elevated MD values could be related to perfusion within the capillaries of the heart when using a reference b-value of 0 s/mm^2 [5]. Moreover, the median FA values reported in our study are on the lower side (0.22-0.58 *unitless*) when comparing to values reported in the literature for spin-echo cDTI [5]. Similar to MD, a possible source of these lower values could be related to perfusion within the capillaries of the heart when using a

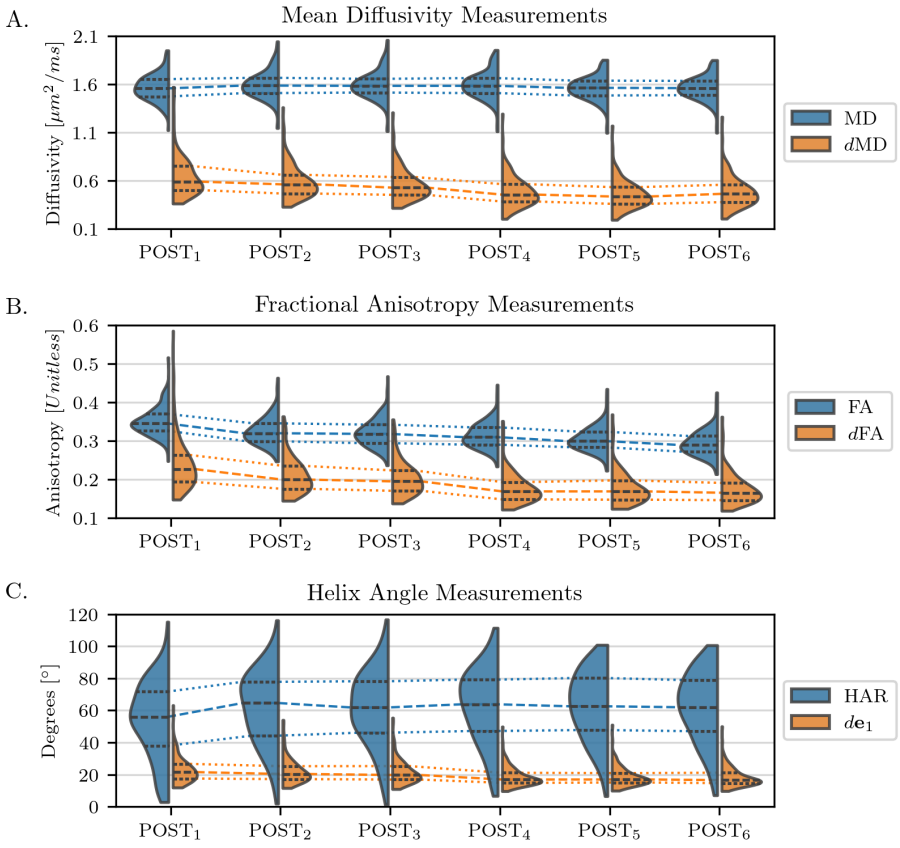

Fig. 4. Split violin plots with median and interquartile range lines for cardiac diffusion tensor imaging (cDTI) metrics and their corresponding uncertainty measurements across all post-processing steps (POSTs). cDTI metrics are characterized by the blue violin plots, while the uncertainty of the corresponding cDTI metrics are characterized by the orange violin plots. cDTI metrics and uncertainty measurements are visualized for: (A) mean diffusivity (MD) and MD uncertainty (dMD); (B) fractional anisotropy (FA) and FA uncertainty (dFA); and (C) helix angle range (HAR) and the primary eigenvector uncertainty ($d\boldsymbol{e}_1$).

reference b-value of 0 s/mm^2 [5]. This decrease in FA across all POSTs while the data quality improves with each incremental POST, suggests that factors that decrease sources of measurement discrepancy (e.g., noise) tend to decrease FA [9]. The median HAR in our study is below the expected range (95°-110°) when compared to values typically reported in the literature for spin-echo cDTI [5]. In our data, we tend to see that HA values are more shallow (lower overall angle magnitude) near the epicardial border than anticipated, thus reducing our HAR. While it is possible for absolute sheetlet angle (E2A) to be calculated for

motion-compensated spin-echo acquisitions, the short time between paired diffusion encoding gradients (Δ) and the comparatively long duration of the diffusion encoding gradient (δ) has led to observations of less reliable results when compared to stimulated acquisition mode (STEAM) [26,15]. STEAM acquisitions have a long Δ and a short δ, which has been hypothesized to increase reliability of the E2A metric. Due to the less reliable nature of E2A for motion-compensated spin echo acquisitions, these results were intentionally not reported.

cDTI is an emerging technology for which many experimental variables are still being investigated. In particular, substantial work continues to explore the impacts of pulse sequences, spatial resolution, and MRI gradient hardware on cDTI metrics. The goal is to identify the approaches that objectively and accurately estimate cDTI metrics. Improvements in MRI software and hardware will continue to evolve and the approach outlined herein provides one framework for understanding the impact of different post-processing steps on the acquired data. While the MD and FA results are converging within the literature, there remains a discordance between the expected helix angle range seen on histology and that obtained with cDTI.

As for limitations, within some of the CarDpy modules, different algorithms could have been used for data processing. For example, within the Denoising module, algorithms such as non-local means denoising [7] or "Patch2Self" denoising [8] could have been implemented over local PCA denoising. Additionally, our current study reconstructs tensors using averaging as a default module to inherently improve the SNR, although individual measurements (before averaging) could have also been used for the tensor reconstruction. The use of individual measurements for the tensor reconstruction may provide benefits in terms of resilience to noise and preserving finer structural information, but requires a modified approach to characterize the uncertainty in cDTI parametric maps. Furthermore, it is difficult to predict if the same level of improvements will be present on cDTI data acquired with high performance ($G_{max} = 80$ mT/m, $S_{max} = 200$ T/m/s) or ultra-high performance ($G_{max} = 200$ mT/m, $S_{max} = 200$ T/m/s) scanners compared to the commodity gradient hardware available for this study ($G_{max} = 45$ mT/m, $S_{max} = 200$ T/m/s). Future work can use the approach outlined herein to understand the impact of various acquisition strategies across different scanners and across different open-source cDTI post-processing software packages.

5 Conclusions

We characterized the effects of several post-processing steps on cDTI metrics (MD, FA, and HAR) and the corresponding uncertainties (dMD, dFA, and $d\boldsymbol{e}_1$) in a cohort of healthy volunteers. We observed that registration (POST_2) and shot-rejection (POST_4) were the POSTs that most improved cDTI metrics and uncertainties. The gains from registration (POST_2) were observed in the HAR, while the gains from shot-rejection were observed in the remaining cDTI metrics (MD and FA) and across all reported uncertainties.

Acknowledgments. This study was supported, in part, by AHA.23PRE1018442 to AJH, NSF 2205043 to LEP, NIH R01 HL131823 to DBE, NIH R01 HL152256 to DBE, and NSF 2205103 to DBE.

Disclosure of Interests. The authors have no competing interests to declare that are relevant to the content of this article.

Accepted Version This version of the contribution has been accepted for publication, after peer review but is not the Version of Record and does not reflect post-acceptance improvements, or any corrections. The Version of Record is available online at: http://dx.doi.org/10.1007/978-3-031-94562-5_13. Use of this Accepted Version is subject to the publisher's Accepted Manuscript terms of use https://www.springernature.com/gp/open-research/policies/accepted-manuscript-terms.

References

1. Aliotta, E., Moulin, K., Magrath, P., Ennis, D.B.: Quantifying precision in cardiac diffusion tensor imaging with second-order motion-compensated convex optimized diffusion encoding. Magnetic resonance in medicine **80**(3), 1074–1087 (2018)
2. Aliotta, E., Wu, H.H., Ennis, D.B.: Convex optimized diffusion encoding (code) gradient waveforms for minimum echo time and bulk motion–compensated diffusion-weighted mri. Magnetic resonance in medicine **77**(2), 717–729 (2017)
3. Bernstein, M.A., Fain, S.B., Riederer, S.J.: Effect of windowing and zero-filled reconstruction of mri data on spatial resolution and acquisition strategy. Journal of magnetic resonance imaging: an official journal of the international society for magnetic resonance in medicine **14**(3), 270–280 (2001)
4. Cork, T.E., Perotti, L.E., Verzhbinsky, I.A., Loecher, M., Ennis, D.B.: High-resolution ex vivo microstructural mri after restoring ventricular geometry via 3d printing. In: Functional Imaging and Modeling of the Heart: 10th International Conference, FIMH 2019, Bordeaux, France, June 6–8, 2019, Proceedings 10. pp. 177–186. Springer (2019)
5. Dall'Armellina, E., Ennis, D.B., Axel, L., Croisille, P., Ferreira, P.F., Gotschy, A., Lohr, D., Moulin, K., Nguyen, C.T., Nielles-Vallespin, S., et al.: Cardiac diffusion-weighted and tensor imaging: A consensus statement from the special interest group of the society for cardiovascular magnetic resonance. Journal of Cardiovascular Magnetic Resonance **27**(1), 101109 (2025)
6. Davidson, R., MacKinnon, J.G.: Bootstrap tests: How many bootstraps? Econometric Reviews **19**(1), 55–68 (2000)
7. Descoteaux, M., Wiest-Daesslé, N., Prima, S., Barillot, C., Deriche, R.: Impact of rician adapted non-local means filtering on hardi. In: International Conference on Medical Image Computing and Computer-Assisted Intervention. pp. 122–130. Springer (2008)
8. Fadnavis, S., Batson, J., Garyfallidis, E.: Patch2self: Denoising diffusion mri with self-supervised learning. Advances in Neural Information Processing Systems **33**, 16293–16303 (2020)
9. Gahm, J.K., Kindlmann, G., Ennis, D.B.: The effects of noise over the complete space of diffusion tensor shape. Medical image analysis **18**(1), 197–210 (2014)

10. Gamper, U., Boesiger, P., Kozerke, S.: Diffusion imaging of the in vivo heart using spin echoes–considerations on bulk motion sensitivity. Magnetic Resonance in Medicine: An Official Journal of the International Society for Magnetic Resonance in Medicine **57**(2), 331–337 (2007)
11. Garyfallidis, E., Brett, M., Amirbekian, B., Rokem, A., Van Der Walt, S., Descoteaux, M., Nimmo-Smith, I., Contributors, D.: Dipy, a library for the analysis of diffusion mri data. Frontiers in neuroinformatics **8**, 8 (2014)
12. Griswold, M.A., Jakob, P.M., Heidemann, R.M., Nittka, M., Jellus, V., Wang, J., Kiefer, B., Haase, A.: Generalized autocalibrating partially parallel acquisitions (grappa). Magnetic Resonance in Medicine: An Official Journal of the International Society for Magnetic Resonance in Medicine **47**(6), 1202–1210 (2002)
13. Jones, D.K.: Determining and visualizing uncertainty in estimates of fiber orientation from diffusion tensor mri. Magnetic Resonance in Medicine: An Official Journal of the International Society for Magnetic Resonance in Medicine **49**(1), 7–12 (2003)
14. Kellner, E., Dhital, B., Kiselev, V.G., Reisert, M.: Gibbs-ringing artifact removal based on local subvoxel-shifts. Magnetic resonance in medicine **76**(5), 1574–1581 (2016)
15. Khalique, Z., Scott, A.D., Ferreira, P.F., Nielles-Vallespin, S., Firmin, D.N., Pennell, D.J.: Diffusion tensor cardiovascular magnetic resonance in hypertrophic cardiomyopathy: a comparison of motion-compensated spin echo and stimulated echo techniques. Magnetic Resonance Materials in Physics, Biology and Medicine **33**, 331–342 (2020)
16. Kingsley, P.B.: Introduction to diffusion tensor imaging mathematics: Part iii. tensor calculation, noise, simulations, and optimization. Concepts in magnetic resonance part A **28**(2), 155–179 (2006)
17. Kung, G.L., Vaseghi, M., Gahm, J.K., Shevtsov, J., Garfinkel, A., Shivkumar, K., Ennis, D.B.: Microstructural infarct border zone remodeling in the post-infarct swine heart measured by diffusion tensor mri. Frontiers in physiology **9**, 826 (2018)
18. Lohr, D., Terekhov, M., Veit, F., Schreiber, L.M.: Longitudinal assessment of tissue properties and cardiac diffusion metrics of the ex vivo porcine heart at 7 t: Impact of continuous tissue fixation using formalin. NMR in Biomedicine **33**(7), e4298 (2020)
19. Magat, J., Yon, M., Bihan-Poudec, Y., Ozenne, V.: A groupwise registration and tractography framework for cardiac myofiber architecture description by diffusion mri: an application to the ventricular junctions. Plos one **17**(7), e0271279 (2022)
20. Manjón, J.V., Coupé, P., Concha, L., Buades, A., Collins, D.L., Robles, M.: Diffusion weighted image denoising using overcomplete local pca. PloS one **8**(9), e73021 (2013)
21. Moulin, K., Croisille, P., Feiweier, T., Delattre, B.M., Wei, H., Robert, B., Beuf, O., Viallon, M.: In vivo free-breathing dti and ivim of the whole human heart using a real-time slice-followed se-epi navigator-based sequence: A reproducibility study in healthy volunteers. Magnetic resonance in medicine **76**(1), 70–82 (2016)
22. Moulin, K., Stoeck, C.T., Axel, L., Broncano, J., Croisille, P., Dall'Armellina, E., Ennis, D.B., Ferreira, P.F., Gotschy, A., Miro, S., et al.: In vivo cardiac diffusion imaging without motion-compensation leads to unreasonably high diffusivity. Journal of Magnetic Resonance Imaging **58**(6), 1990–1991 (2023)
23. Neto Henriques, R.: Advanced methods for diffusion MRI data analysis and their application to the healthy ageing brain. Ph.D. thesis, University of Cambridge (2018)

24. Nielles-Vallespin, S., Scott, A., Ferreira, P., Khalique, Z., Pennell, D., Firmin, D.: Cardiac diffusion: technique and practical applications. Journal of Magnetic Resonance Imaging **52**(2), 348–368 (2020)
25. Pashakhanloo, F., Herzka, D.A., Mori, S., Zviman, M., Halperin, H., Gai, N., Bluemke, D.A., Trayanova, N.A., McVeigh, E.R.: Submillimeter diffusion tensor imaging and late gadolinium enhancement cardiovascular magnetic resonance of chronic myocardial infarction. Journal of Cardiovascular Magnetic Resonance **19**(1), 9 (2016)
26. Scott, A.D., Nielles-Vallespin, S., Ferreira, P.F., Khalique, Z., Gatehouse, P.D., Kilner, P., Pennell, D.J., Firmin, D.N.: An in-vivo comparison of stimulated-echo and motion compensated spin-echo sequences for 3 t diffusion tensor cardiovascular magnetic resonance at multiple cardiac phases. Journal of cardiovascular magnetic resonance **20**(1), 1 (2018)
27. Stoeck, C.T., von Deuster, C., Genet, M., Atkinson, D., Kozerke, S.: Second-order motion-compensated spin echo diffusion tensor imaging of the human heart. Magnetic resonance in medicine **75**(4), 1669–1676 (2016)
28. Stoeck, C.T., Scott, A.D., Ferreira, P.F., Tunnicliffe, E.M., Teh, I., Nielles-Vallespin, S., Moulin, K., Sosnovik, D.E., Viallon, M., Croisille, P., et al.: Motion-induced signal loss in in vivo cardiac diffusion-weighted imaging. Journal of magnetic resonance imaging: JMRI **51**(1), 319 (2019)
29. Streeter Jr, D.D., Bassett, D.L.: An engineering analysis of myocardial fiber orientation in pig's left ventricle in systole. The Anatomical Record **155**(4), 503–511 (1966)
30. Streeter Jr, D.D., Spotnitz, H.M., Patel, D.P., Ross Jr, J., Sonnenblick, E.H.: Fiber orientation in the canine left ventricle during diastole and systole. Circulation research **24**(3), 339–347 (1969)
31. Wilson, A.J., Sands, G.B., LeGrice, I.J., Young, A.A., Ennis, D.B.: Myocardial mesostructure and mesofunction. American Journal of Physiology-Heart and Circulatory Physiology **323**(2), H257–H275 (2022)